https://doi.org/10.1016/j.jmst.2021.04.074

Combining gradient structure and supersaturated solid solution to achieve superior mechanical properties in WE43 magnesium alloy

Wanting Sun[a], Bo Wu[a], Hui Fu[a], Xu-Sheng Yang[a,b*], Xiaoguang Qiao[d], Mingyi Zheng[d**], Yang He[e], Jian Lu[f], San-Qiang Shi[c***]

[a]*State Key Laboratory of Ultra-precision Machining Technology, Department of Industrial and Systems Engineering, The Hong Kong Polytechnic University, Hung Hom, Hong Kong, China (E-mail: xsyang@polyu.edu.hk)*

[b]*Hong Kong Polytechnic University Shenzhen Research Institute, Shenzhen, China*

[c]*Department of Mechanical Engineering, The Hong Kong Polytechnic University, Hung Hom, Hong Kong, China (E-mail: mmsqshi@polyu.edu.hk)*

[d]*School of Materials Science and Engineering, Harbin Institute of Technology, Harbin 150001, China (E-mail: zhenghe@hit.edu.cn)*

[e]*Centre for Composite Materials and Structures, Harbin Institute of Technology, Harbin 150080, China*

[f]*Department of Mechanical Engineering, City University of Hong Kong, Kowloon, Hong Kong, China*

Abstract:

In this study, surface mechanical attrition treatment is employed to produce successfully a gradient nanostructured layer on WE43 magnesium alloy. X-ray diffraction, energy dispersive X-ray spectrometer, and high-resolution transmission electron microscope observations are mainly performed to uncover the microstructure evolution responsible for the refinement mechanisms. It reveals that the grain refinement process consists of three transition stages along the depth direction from the core matrix to the topmost surface layer, i.e., dislocation cells and pile-ups, ultrafine subgrains, and randomly orientated nanograins with the grain size of ~40 nm. Noticeably, the original Mg_3RE second phase is also experienced refinement and then re-dissolved into the α-Mg matrix phase, forming a supersaturated solid solution nanostructured α-Mg phase in the gradient refined layer. Due to the cooperative effects of grain refinement hardening, dislocation hardening, and supersaturated solid-solution hardening, the gradient nanostructured WE43 alloy contributes to the ultimate tensile strength of ~435 MPa and ductility of ~11.0 %, showing an extraordinary strain hardening and mechanical properties among the reported severe plastic deformation-processed Mg alloys. This work provides a new strategy for the optimization of mechanical properties of Mg alloys via combining the gradient structure and supersaturated solid solution.

Key words: Mg-RE alloy; surface mechanical attrition treatment; gradient nanostructure; supersaturated solid solution; high strength and ductility; strengthening mechanisms

* Corresponding author. xsyang@polyu.edu.hk (X.-S Yang). Tel: +852-2766 6604

** Corresponding author. zhenghe@hit.edu.cn (M.-Y Zheng)

*** Corresponding author. mmsqshi@polyu.edu.hk (S.-Q Shi)

1. Introduction

Owing to the advantages of low density, high specific strength and stiffness, and good castability, etc., magnesium (Mg) alloys have received considerable attention in various industrial applications, especially in automotive, railway transit and hydrogen storage industries [1-5]. With the addition of rare-earth (RE) elements, particularly, the formed Mg-RE alloys can provide the strengthening effects of solid solution and/or thermal stable second phases, thus leading to the superior mechanical properties both at room and elevated temperatures to the conventional Mg alloys [6-8]. Generally, the as-cast Mg-RE alloys are composed of extremely coarse matrix grains and eutectic compounds formed during the solidification [9]. Therefore, micro-cracks/ voids are still easily nucleated at the interfaces between these second phases and coarse-grained (CG) matrix to degrade their mechanical properties. Accordingly, mechanical properties of Mg-RE alloys are usually improved by grain refinement methods via tailoring the dislocation nucleation and interactions, such as hot rolling, hot extrusion [7, 10-12], and various severe plastic deformation (SPD) techniques [13]. However, the strengthened homogeneous nanograined metals are accompanied by the sacrifice of ductility, due to the severely suppressed dislocation activities [14]. Alternatively, various surface severe plastic deformation (SSPD) techniques, such as surface mechanical attrition treatment (SMAT), laser shock processing, shot peening, and surface mechanical grinding treatment (SMGT), etc., have been developed in recent years to construct a unique architecture-heterogeneous gradient nanostructure, e.g., gradient phases/composition/grain size, which can result in the high strength-ductility synergy. The superior combination of high strength-ductility can be realized by an extra overall strain hardening deriving from the strain partitioning and stress transfer in the gradient nanostructures at different depth layers [14, 15].

The refinement process and corresponding plastic deformation mechanisms of the SSPD-processed materials have been investigated widely for some Mg alloys [16-26]. For example, a better strength-ductility synergy was achieved in SSPD-processed AZ31 alloy [18], due to the alleviated deformation localization and suppressed strain concentration in the gradient nanostructure [19, 20]. In particular, the crystallographic orientation was also found to be changed gradually along the depth direction of the SMAT-processed AZ31 alloys with pre-rolling [21, 22] and pre-hot-forging [23], respectively, in which the refined layers exhibited weaker textures as the activation of non-basal slips accordingly. Meanwhile, the refinement progress of SSPD-processed AZ91D solid solution-treated

alloy was divided into three steps, i.e., deformation twinning, formation of subgrains, and dynamic recrystallization without any precipitation [24]. However, the grain refinement of as-cast AZ91D alloy during the SMAT process was reported to be associated with the dislocation activities without twinning. The suppression of twinning in Mg alloys might be due to the change of c/a ratio, as reported in SMAT processing of as-rolled Mg-3Li-6Al (wt.%) alloy [27]. More interestingly, it was revealed that the enhanced surface microhardness of SSPD-processed AZ91D alloy was attributed to the grain refinement accompanying the re-dissolution of the β-$Mg_{17}Al_{12}$ second phase into the α-Mg matrix [25, 26]. Similarly, the re-dissolution of the Mg_2Ca second phase into the α-Mg matrix was also reported in the SSPD-processed as-cast Mg-1Ca (wt.%) alloy [28]. It was also found that the second phases in the SMAT processing of as-cast and aged Mg-7Al-2Sn (wt.%) alloys can provide the sites for activating dislocations and inhibition of twinning [29]. Noticeably, the addition of RE elements into Mg alloys could also promote the non-basal slips of HCP crystals [30], which may decrease the plastic anisotropy and improve the plasticity for the formation of randomly orientated nanograins during the grain refinement process. It was reported that the tensile yield strength of SMAT-processed Mg-3Gd (wt.%) alloy was increased from the original 128.2 MPa to 152.4 MPa [31]. The improved wear resistance of SMAT-processed Mg-6Gd-3Y-0.5Zr (wt.%) alloy and the promoted precipitation behavior of SMAT-processed Mg-10Gd-3Y-0.4Zr (wt.%) alloy have also been documented [32, 33], respectively. These divergent experimental results reflect that grain refinement and corresponding enhanced mechanical properties of SSPD-induced gradient nanostructured Mg-RE alloys. Nonetheless, one might note that the enhancement in tensile yield strength of SMAT-processed Mg-Gd alloy is still limited. Meanwhile, there is also an absence of information about re-dissolution of RE atoms into Mg matrix for hardening these mentioned Mg-RE alloys. This might be due to the lack of the suitable second phase containing RE atoms in these Mg-RE alloys and/or the detailed microstructural examinations. WE43 is a typical high-strength Mg-RE alloy that possesses good mechanical and corrosion properties both at ambient and elevated temperatures, exhibiting excellent potential applications such as aerospace sectors and biodegradable implants[34, 35]. In addition, it has also been reported that Mg_3RE eutectic compound is a common second phase in WE43 alloy [36, 37]. Therefore, it is possible and meaningful to investigate the effects of gradient nanostructuring and re-dissolution of the Mg-RE second phase on the mechanical properties of WE43 alloy produced by SSPD techniques.

In this study, we use the SMAT technique to successfully produce the gradient nanostructured

layer on the commercial Mg-RE alloy, i.e., WE43 alloy with the Mg_3RE second phase. The microstructural evolution for the grain refinement process is mainly dissected by the high-resolution transmission electron microscopy (HRTEM) observations, revealing that the formation of gradient nanostructured layer consists of dislocation cells and pile-ups, ultrafine subgrains, and randomly nanograins with the grain size of ~40 nm along the direction from the inner matrix to surface. Particularly, the dissolution of the RE-containing second phase into the α-Mg matrix is found during the SMAT process, leading to the supersaturated solid solution involved in the gradient nanostructure. Accordingly, the SMAT-processed WE43 alloy shows superior mechanical properties with the ultimate tensile strength of ~435 MPa and ductility of 11.0 %. Moreover, the hardening effects deriving from the grain boundary, high dislocation density, and supersaturated solid solution are estimated to quantitatively fully understand the overall plastic strengthening mechanisms of SMAT-processed WE43 alloy along the depth direction. Our findings offer a new strategy for the optimization of Mg-RE alloys with an excellent comprehensive mechanical performance.

2. Experimental procedures

The original WE43 sheet with the composition listed in Table 1 was hot extruded at a temperature of 450 ^{o}C with a ratio of 40 and ram speed of 0.1 mm/s. The as-extruded WE43 alloy sheet with a thickness of 1.5 mm was subjected to SMAT processing at an ambient temperature for 10 min with a vibrating frequency of 20 kHz using stainless steel balls with diameter of 3 mm. It should be noted that the SMAT process was stopped 30 s after every 1 min-treatment to avoid a substantial temperature increment of specimen.

Table 1 Measured chemical composition of as-extruded WE43 alloy

Elements	Mg	Y	Nd	Gd	Zr
Concentrations (wt.%)	Bal.	4.20	2.30	1.44	0.53

The microstructure of the WE43 alloys before and after the SMAT process was observed using Olympus D11 optical microscope (OM), a JEOL JSM-7000F field-emission scanning electron microscope (FE-SEM), and an FEI JEM-2100F transmission electron microscope (TEM) operated at an accelerating voltage of 200 kV. The quantitative analysis of the chemical compositions of the second phase in the alloy was conducted on an energy dispersive X-ray spectrometer (EDS) equipped on FE-SEM. The texture of the as-extruded plate was analyzed by an EDAX-TSL electron backscattered diffraction (EBSD) system operating at 25 kV, equipped with OIM Analysis software The phase

constituent of the SMAT-processed specimens were performed on an X′Pert PRO X-ray diffractometer. The phase diagram and phase volume fraction and variation of solid solubility of solute atoms with temperature under 1 atm were calculated using Pandat^{TM} (Compu Therm LLC) with the latest PanMg database. The Materials Analysis Using Diffraction (MAUD) software was applied for analyzing the X-ray diffractometry (XRD) patterns to evaluate the crystallite size D_c and microstrain ε of different depth layers in the SMAT-deformed sample [38, 39]. A detailed description of this method has been provided in previous references [38-40], and the dislocation density ρ can be calculated using the equation of $\rho = \frac{2\sqrt{3}\langle\varepsilon^2\rangle^{1/2}}{D_c b}$ [40], where b is the Burgers vector. Based on the OM observations, XRD analysis, and the variation of hardness along the depth direction in the hardness tests, plane-view TEM observations were conducted at different depth layers of the SMAT-processed specimens to study the sequential evolutions of the microstructure and grain size. For the plane-view TEM observation at a certain depth layer, we first mechanically polished the specimen from the topmost surface side to achieve this depth layer. Then, this specimen was mechanically polished from the opposite side, forming a ~25 μm-thick TEM foil. After that, the TEM foil was glued to the copper ring for the further single-side ion milling on the precision ion polishing system Gatan 691. The single-side ion milling mode was also conducted to thin the TEM foil from the opposite side of the observation layer. Consequently, the damage of the target observed depth layer during the ion milling process can be avoided for the TEM observations. Finally, the plane-view TEM observations were performed on this depth layer from the topmost surface-side direction.

The distribution of Vickers microhardness along the depth direction of the SMAT-processed WE43 alloy was tested using a Zwick microhardness tester under a constant load of 500 gf for 15 s. Each reported hardness value is taken an average of ten separated indentions. The tensile specimens of as-extruded and SMAT-processed alloys with a gauge length of 15 mm and cross-section of 1.5 × 6 mm^2 were prepared by electrical discharge machining. However, the tensile specimen thickness of gradient layer was designed to be ~200 μm by mechanical polishing, according to the OM observations and hardness measurements. All the uniaxial tensile tests in the present work were carried out at an ambient temperature by an Instron 5569 universal test machine with a crosshead speed of 1 mm/min.

3. Results and analysis

3.1 Microstructure observation of as-extruded WE43 alloy

Fig.1 shows the microstructure characteristics of as-extruded WE43 alloy. It can be seen from Fig. 1(a) that equiaxed and fine-grained microstructure with an average grain size of ~17 μm is produced by hot extrusion at 450 °C, suggesting that almost complete dynamic recrystallization (DRX) during such thermomechanical process. Further examination by SEM image in Fig. 1(b) shows a few of broken-up block-shaped eutectic phases stretched like a necklace structure along extrusion direction (ED), with particle sizes ranging between 2-10 μm as indicated in the inset. The EDS analysis of second phase particles of bright contrast marked by arrows is given in Fig. 1(c). Based on the analysis of chemical compositions in conjunction with previous reports [36, 37], it allows for the identification of these intermetallic compounds to be β-Mg_3RE type equilibrium phase with a face-centered cubic (FCC) crystal structure. It deviates from several other Mg-RE compounds with different atomic ratios calculated by thermodynamic modelling, as shown Fig. 2, which is due to the ideal equilibrium state applied in thermodynamic modelling. It has also been reported that Mg_3RE eutectic compound is usually regarded as a common stable phase in WE43 alloy [36, 37]. Noticeably, the volume fraction of the Mg_3RE second phase is approximately estimated to be 7.2% by analysis of SEM images, which is slightly higher than the total value of these Mg-RE second phases calculated by thermodynamic modelling using the PanMg database as shown in Fig. 2(b). Meanwhile, the α-Mg matrix contains the compositions of 3.81 wt.%Y, 0.83 wt.%Gd, and 1.05 wt.%Nd, which are a slightly lower than those of the equilibrium solubility of solutes at 450 °C (see Fig.1(d) and Fig.2(c)). This can be explained by the fact that some RE atoms can be dissolved thus close to being saturated in the α-Mg matrix through the pre-extrusion, homogenization treatment, and plastic deformation at elevated temperature. The grain orientation of the as-extruded WE43 sheet was revealed in the inverse pole figure (IPF) map obtained from the ED-TD plane as shown in Fig. 1(e). The mean grain sizes detected by OM and EBSD methods are coincident, suggesting that there is complete DRX with high-angle boundaries having misorientation angles >15° during extrusion. According to the EBSD analysis of pole figures, it can be clearly observed that the as-extruded WE43 sheet exhibits a typical fiber texture with (0001) basal planes parallel to the extrusion direction (ED), while the intensity of basal texture is moderate weak as a result of the large volume fraction of DRXed grains with random orientation formed at elevated deformation temperature of 450 °C. It is noteworthy that the addition of RE elements into Mg alloys also causes the texture weakening driven by the particles stimulated nucleation (PSN) [41] and the strong interaction of solutes with dislocations and grain boundaries [42].

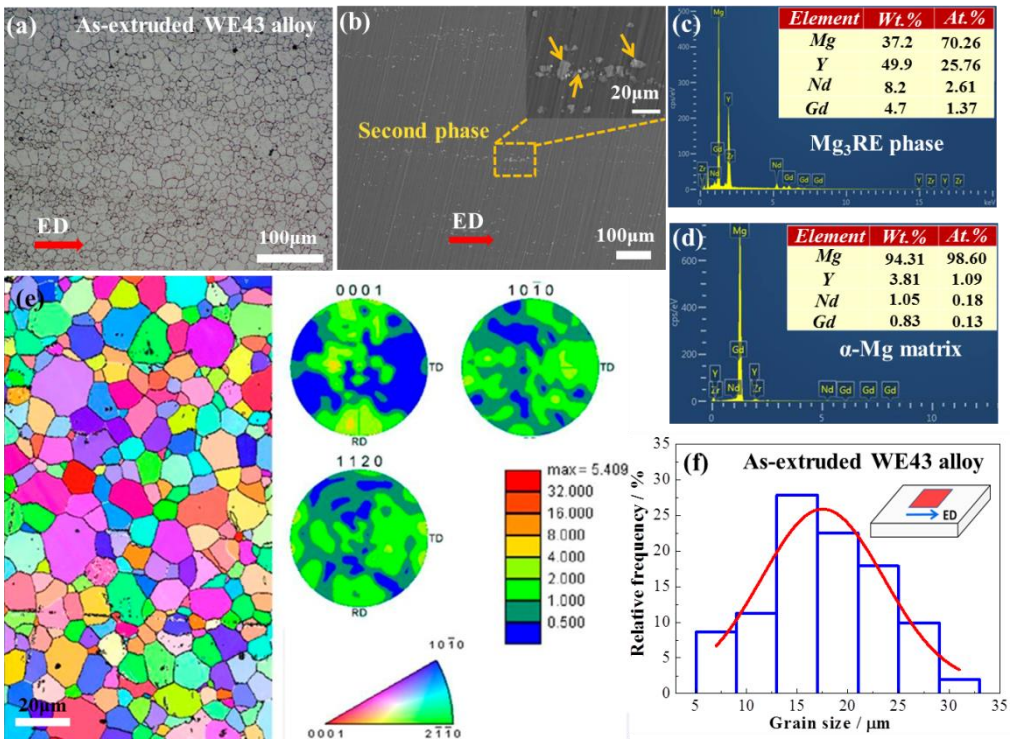

Fig.1 Microstructure analysis of as-extruded WE43 alloy: (a) OM; (b) SEM image; (c) EDS results of second phase marked by arrows in Fig. 1(b); (d) EDS results of α-Mg matrix; (e) EBSD analysis and (f) histogram for the distribution of grain size.

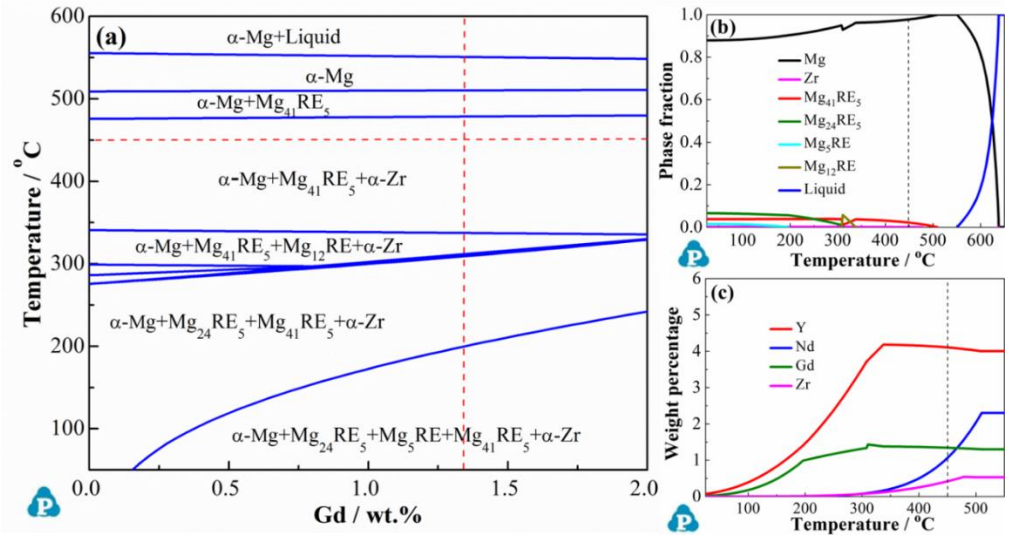

Fig.2 Results of thermodynamic modelling using the PanMg database (a) Phase diagram of Mg-4.2Y-2.3Nd-xGd-0.53Zr (wt.%) alloy; (b) Dependence of equilibrium phase fraction of WE43 alloy on temperature under 1 atm and (c) Variation of solid solubility of solutes with temperature under 1 atm.

3.2 Microstructure observations of SMAT-processed WE43 alloy

3.2.1 OM observation

Fig. 3(a) shows the cross-sectional OM image of SMAT-processed WE43 alloy. Different from the OM microstructure of as-extruded specimen with well-distinguished grain boundaries in Fig. 1(a),

a ~100 μm-thick refined surface layer with obscure grain boundaries can be observed in the SMAT-processed WE43 alloy. Fig. 3(b) and (c) respectively give the enlarged OM images of refined and coarse-grained matrix layers, presenting the formation of the gradient nanostructured layer on the WE43 alloy due to the gradient plastic strain and strain rate along the depth direction during the SMAT process. The layer-by-layer HRTEM observations will be introduced in the next section to show the detailed microstructural evolution for the formation of gradient structural characteristics during the SMAT process.

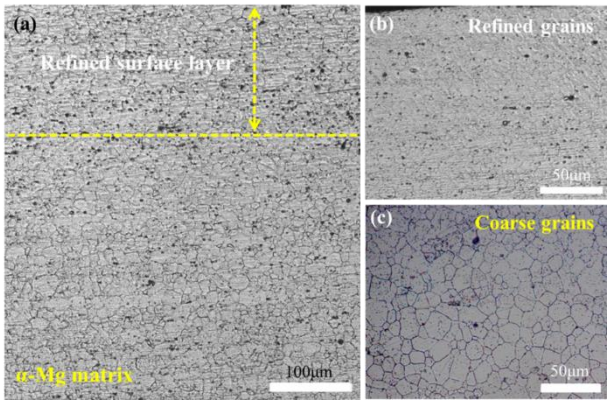

Fig.3 Optical micrographs of cross section of (a) SMAT-processed WE43 alloy; (b) the refined grains of the surface layer and (c) the coarse grains of the WE43 alloy matrix.

3.2.2 XRD analysis

The XRD patterns of SMAT-processed samples at various depth layers are shown in Fig. 4(a), where the XRD pattern of the depth layer of ~300 μm below the top surface can be considered as that of the original as-extruded sample. The characteristic diffraction peaks of the α-Mg matrix and intermetallic compounds of Mg_3(Nd, Y, Gd) phase can be confirmed in the original sample [9], which is in good agreement with EDS results. When the depth layer decreases with increasing strain and strain rate during the SMAT process, there are no prominent diffraction peaks corresponding to the formation of any other new precipitates. In contrast, the diffraction peaks of the Mg_3(Nd, Y, Gd) second phase cannot be indexed starting from the depth layer of ~90 μm. It might be that these second phase particles are gradually broken up and further dissolved into the matrix phase, forming a supersaturated solid solution α-Mg phase. Noticeably, an enlarged XRD pattern ranging from 31^o to 38^o shows that the peaks of α-Mg matrix phase are obviously shifted left to the smaller-angle direction, indicating the increase of the lattice parameters. Moreover, there exists a possibility that the solid solution of RE atoms with larger atomic radius could lead to the lattice distortion and the consequent

change of ratio of *c/a* in the expanded Mg lattice [43, 44]. Therefore, the dissolution of RE atoms into the α-Mg matrix phase should be responsible for such phenomenon [43, 44], which is also evidenced by the evolution of the lattice axial ratio c/a given in Fig. 4(b), suggesting the formation of supersaturated solid solution. In addition, a significant intensity reduction and peak broadening of the α-Mg matrix phase can be apparently observed in Fig. 4(a), which clearly proves the grain refinement and SPD-induced microstrains along the depth direction. The crystallite size and dislocation density are also plotted as a function of the depth from the top surface in Fig. 4(b). As the deformation strains accumulated with the depth reducing, the value of crystallite size is monotonously decreased, while the dislocation density is dramatically increased. The crystallite size and dislocation density reach ~38.2 nm and ~4.5 × 10^{14} m^{-2}, respectively, in the topmost surface layer of the SMAT-processed specimen. Thereby, a gradient nanostructure WE43 alloy is successfully produced due to the gradient deformation progress during the SMAT process.

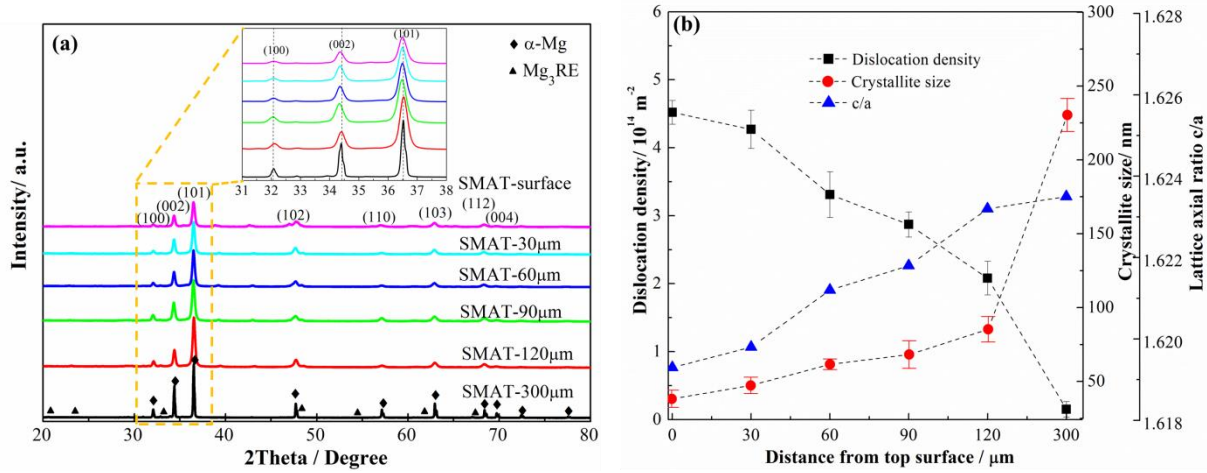

Fig.4 (a) XRD patterns of the SMAT-processed WE43 alloy at various depths from the top surface, and the enlarged section are inserted; (b) crystalline size, dislocation density and lattice axial ratio c/a as a function of the depth from the top surface.

3.2.3 Texture evolution

The texture of the specimen may also be influenced by the gradient strain along depth direction during the SMAT process. The relative diffraction peak intensity is calculated by the following Eq. (1) [45]:

$$J_{hkl} = \frac{I_{hkl}}{I_{100}+I_{002}+I_{101}} \quad (1).$$

While, the normalized peak intensity K_{hkl} is further defined in the following form [45]:

$$K_{hkl} = \frac{J_{hkl,exp}}{J_{hkl,random}} \quad (2),$$

where $J_{hkl,random}$ represents the theoretical maximum relative diffraction peak intensity based on the arbitrarily selected crystal plane of the randomly textured Mg, and $J_{hkl,exp}$ is the calculated relative diffraction peak intensity according to the experimental XRD patterns. Fig. 5 summarizes the evolution of the normalized peak intensities K_{hkl} for three selected major planes of (100), (002) and (101) against depths in SMAT-processed WE43 alloy. The dashed horizontal line with K_{hkl} =1.0 is the referenced intensity level for any major slip planes in theoretical random crystal orientation. As for the depth layer of ~300 μm considered as the original sample without the SMAT process, a slight preferential orientation is reflected from the (002) basal plane (K_{002}＞1) in Fig. 5(a), which is consistent with the EBSD results. When the depth decreases to ~120 μm, the normalized intensity of (002) plane starts to be weakened and approaches the value for a random texture (K_{002}≈1), suggesting that a random texture is developed after the introduction of strains through SMAT. With the depth layers further reduce to ~30 μm and topmost surface, the normalized intensities of these planes remain approximately the same level, suggesting that the produced gradient nanograins should be distributed with random orientation. Besides, the corresponding (0002) pole figures of SMAT-processed WE43 alloy at various depth layers estimated by XRD using Maud software are shown in Fig. 5(b), where a similar texture evolution can be also observed as compared to the plots in Fig. 5(a). It is reasonable that the original basal texture transit to an almost random one in the refined depth layers during the SMAT process, which might be related to the significant grain refinement with the activation of non-basal slipping.

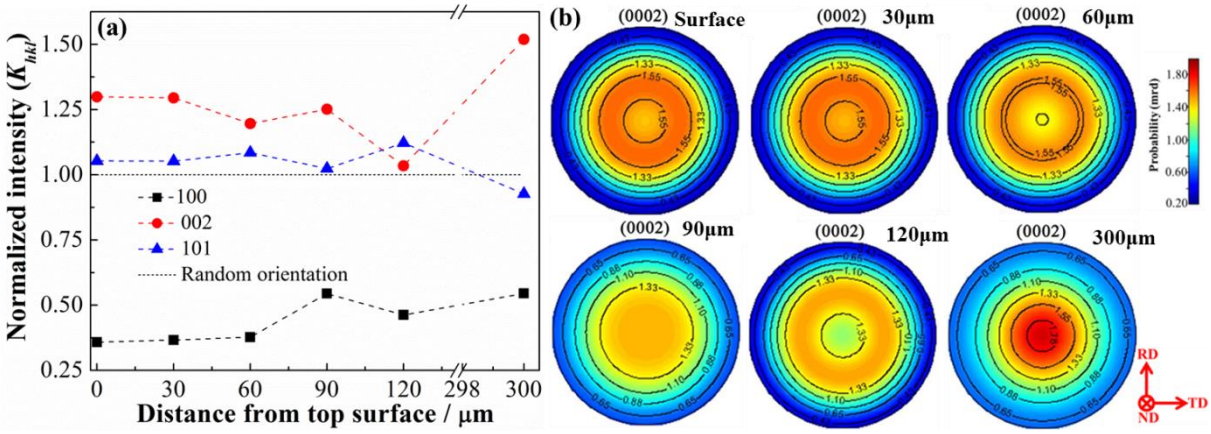

Fig.5 (a) the plots of normalized peak intensity K_{hkl} denpent on the distance from top surface of SMAT-processed WE43 alloy. The dashed horizontal lines indicate the peak intensities for a randomly textured WE43 sample; (b) (0002) Pole figures of SMAT-processed WE43 alloy with various depths from the top surface.

3.2.4 TEM observations

The OM, XRD, and texture analysis suggest consistently that the gradient nanostructured layer is

generated from the depth layer of ~120 μm. Therefore, the detailed HRTEM observations are performed to dissect the microstructural evolution at several representative depth layers from ~ 120 μm to the topmost surface layer of the SMAT-processed WE43 alloy. First, Fig. 6 shows the TEM images of the SMAT-processed WE43 sheet observed at the depth of ~120 μm below the surface. Fig. 6(a-c) are respectively the bright-field image, dark-field image, and corresponding selected area electron diffraction (SAED) patterns at this depth layer, indicating that the grain size is started to be refined to the nanometer level with an average value of ~213 nm as statistical analysis in the inset of Fig. 6(b). The semi-continuous circled SAED patterns in Fig. 6(c) also indicate the grain refinement of α-Mg matrix phase. It should be noticed that there are few isolated diffraction spots marked by rectangle frames in Fig. 6(c), which are indexed as several certain crystalline planes for the residual Mg_3(Nd, Y, Gd) second phase with FCC crystalline structure. The existence of the Mg_3RE phase is further evidenced by the dark-field TEM images in Fig. 6(d) and HRTEM images in Fig. 6(e-f), respectively. The diffraction patterns in Fig. 6(c), HRTEM and corresponding inverse fast Fourier transformation (IFFT) images in Fig. 6(e-f) consistently confirm the lattice constant of the FCC Mg_3RE second phase (i.e., a = 0.735 nm, almost equivalent to the value of 0.74 nm reported in Ref. [37], where RE can be Nd, Gd and/or Y atoms as the little difference in the radius between them [36, 37]. There is no obvious particular orientation relationship and coherent interfacial structure between the Mg_3RE particles and α-Mg matrix, as shown Fig. 6(e). Noticeably, Fig. 6(d) shows that the content of the second phase is significantly decreased, comparing with the original volume fraction ~7.2% in the as-extruded sample by analysis of SEM images. It also shows that these residual Mg_3RE intermetallic compounds are crushed into extremely small nanoparticles. Therefore, the reduction in the Mg_3RE amount might be realized via re-dissolution of RE elements into the α-Mg matrix phase, which is consistent with the XRD analysis in Fig. 4. The EDS analysis in Fig. 6(g) shows the slightly lower concentration of RE solute atoms in the smaller Mg_3RE second-phase particles than that obtained in the as-extruded alloy in Fig. 1(c), which might be connected to the re-dissolution and refinement processes. It should be noted that plenty of typical dislocation cells and dislocation-tangle arrangements emerge inside the heavily deformed grains, as signified by the arrows in Fig. 6(a), inferring that the dislocation activities govern the plasticity for the grain refinement. Specifically, high local stress concentration would induce the dislocation pile-ups at the interface between the Mg_3RE second-phase particles and matrix, which may also result in the dynamic fragmentation and thus the

re-dissolution of the second phase during the SMAT process [25, 26, 28]. Fig. 6(h-j) in detail shows that a serial of lamellar structure with a large aspect ratio generated within the individual matrix grains, implying that high density of the basal plane stacking faults (SFs) existed due to the relatively low stacking fault energy (SFE) in Mg-RE alloys [46]. The corresponding atomic IFFT image in Fig. 6(j) is used to determine the types of SFs and their bounding dislocations. The partial dislocations-induced SFs are usually determined by drawing Burgers circuits around the dislocation cores, where the sense vectors of the dislocations are arbitrarily determined to point into the page and the directions of the Burgers circuits are drawn clockwise following the start-finish/right-handed convention [47, 48]. The closure failure of the Burgers circuit in Fig. 6(j) denotes a $1/6< 20\bar{2}3 >$ Frank partial dislocation, i.e., an interstitial-type I_1 SF in HCP crystal. The introduction of interstitial-type I_1 SF in HCP crystals brings a three-atomic layer of face-centered cubic stacking (ABC), as indicated in Fig. 6(j), converting the stacking sequence from original…ABABAB to…ABABABCBCBCB…. [47, 48]. Specifically, the formation of interstitial-type I_1 SF can be completed through the dislocation reaction of $\frac{1}{2}< 0001 > +\frac{1}{3}< 10\bar{1}0 >\rightarrow \frac{1}{6}< 20\bar{2}3 >$ [47, 48], suggesting that the non-basal slips are activated to refine the grains in this layer [48]. Furthermore, the EDS analysis Fig. 6(k) indicate that the concentration of RE solute atoms slightly increases in the α-Mg matrix at this refined depth layer, which should be attributed to the partial re-dissolution of the second phase.

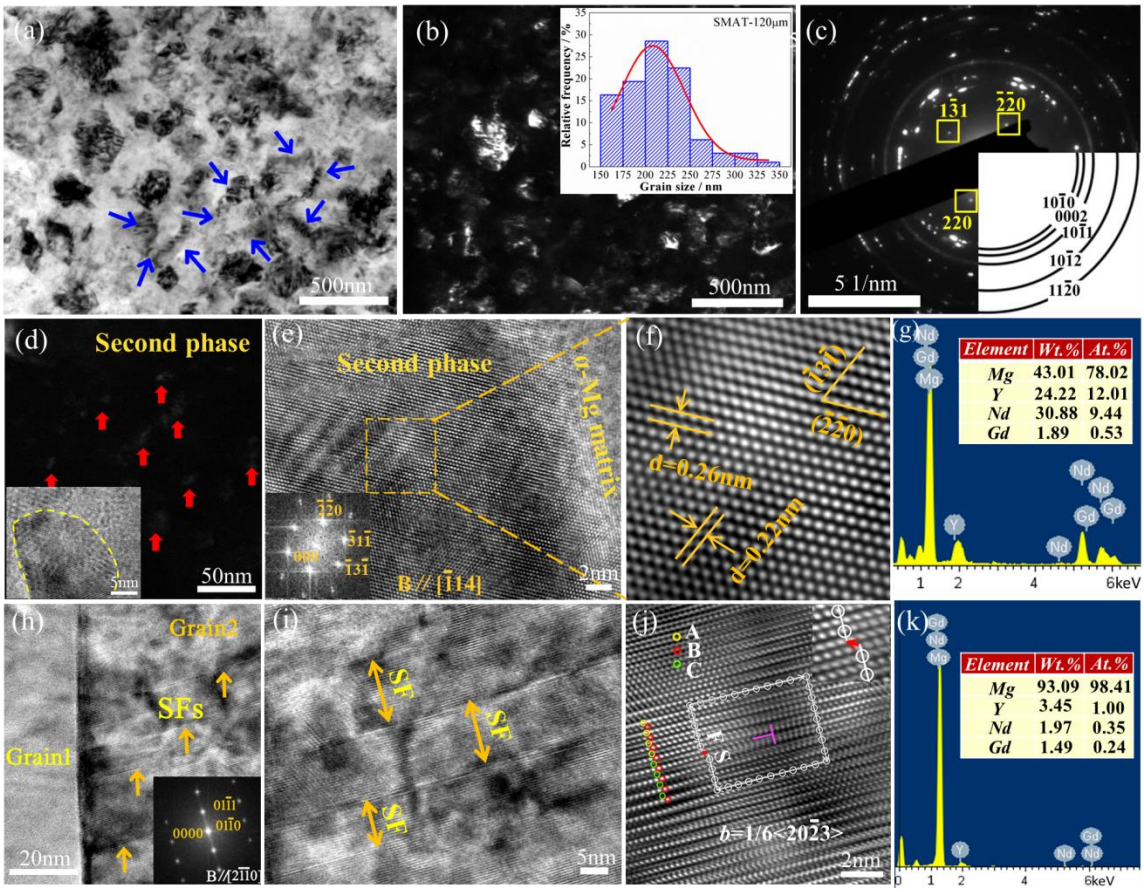

Fig. 6 Microstructure of the SMAT-processed WE43 sheet observed at the depth of 120 μm below the surface: (a) TEM bright field image; (b) TEM dark field image and histogram of distribution of grain size inserted; (c) The corresponding SAED pattern of (a); (d) TEM dark field image of residual intermetallic compounds and the corresponding TEM bright field image inserted; (e) HRTEM image of intermetallic compound and fast Fourier transform (FFT) image inserted; (f) IFFT image of the region marked in (e); (g) EDS analysis of remained second phase particle; (h) TEM image of SFs and the IFFT image inserted; (i) magnified image of (h); (j) IFFT image of SF, and (k) EDS analysis of α-Mg matrix.

Fig. 7 shows the TEM images observed at the depth layer of ~90 μm below the surface in the SMAT-processed WE43 alloy, denoting a further refined average grain size of ~135 nm on the basis of the statistical histogram inserted in Fig. 7(b). It can be noticed in Fig. 7(a) that strain contrasts within the ultrafine grains are non-uniform, suggesting that high-density dislocations and defects are produced by SMAT. The SAED patterns inserted in Fig. 7(a) are composed of elongated arcs of diffraction spots situated around the discontinuity of rings, which is indicative of the subgrains with small misorientations in this layer [49]. Apart from the α-Mg crystalline rings, no additional diffraction spots for the second phase can be found anymore, implying that the second phase nanoparticles are completely re-dissolved into the α-Mg matrix phase with accumulating strains. This demonstrates that the supersaturated solid solution α-Mg phase is obtained, consistent with our XRD results. It is also

supported by EDS analysis as shown in Fig. 7(f), in which the concentration of RE solute atoms in the α-Mg matrix are obviously higher than those in the as-extruded alloy as well as equilibrium state calculated in Fig. 2. Fig. 7(c-e) shows that a high density of non-basal slips-correlated interstitial-type I_1 SFs can also be observed within these subgrains in this depth layer.

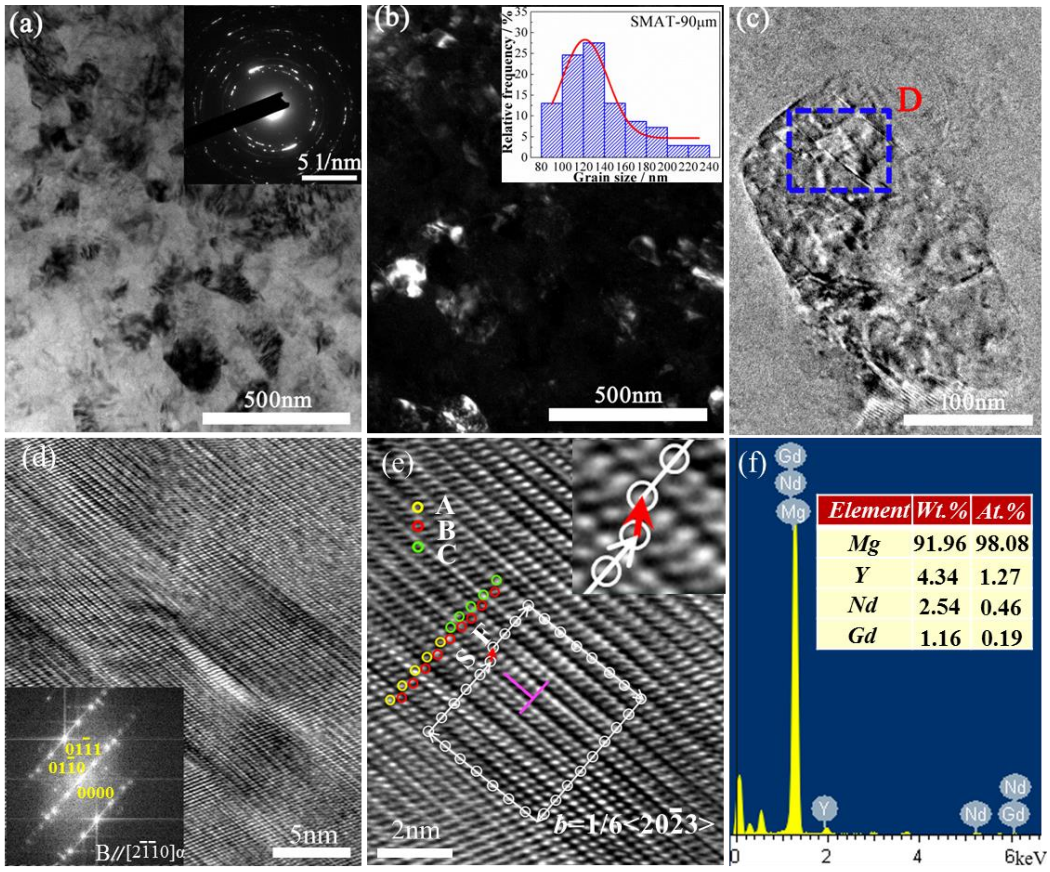

Fig.7 Microstructure of the SMAT-processed WE43 sheet observed at the depth of ~90 μm below the surface: (a) TEM bright field image and the corresponding SAED patterns inserted; (b) TEM dark field image and histogram of distribution of grain size inserted; (c) TEM bright field image of individual refined grain; (d) TEM image of SFs marked by box in (c) and FFT image inserted; (e) IFFT image of SF; (f) EDS analysis of α-Mg matrix.

Fig. 8 gives the TEM images observed at the depth layer ~60 μm below the surface of SMAT-processed WE43 alloy with continually increased strain/strain rate, showing a significant grain refinement with an average grain size of ~96.0 nm through statistical measurements in Fig. 8(b). Typical nanograins in this layer are successfully gradually transited from the ultrafine grains in the depth layer of ~ 120 μm. Moreover, a more uniform distributed SAED pattern with continuous rings in Fig. 8(a) reveals that the misorientations between these nanograins become larger, increasing the percentage of nanograins with high-angle grain boundaries. The non-basal slips-correlated interstitial-type I_1 SFs are still existed within nanograins, according to the HRTEM and corresponding IFFT

images given in Fig. 8(c-e). As seen in Fig. 8(c), it is also evident that such nanograin has curved with irregular boundary, which is resulted from distortions and bending of the lattice fringes induced by high density of dislocations [49].

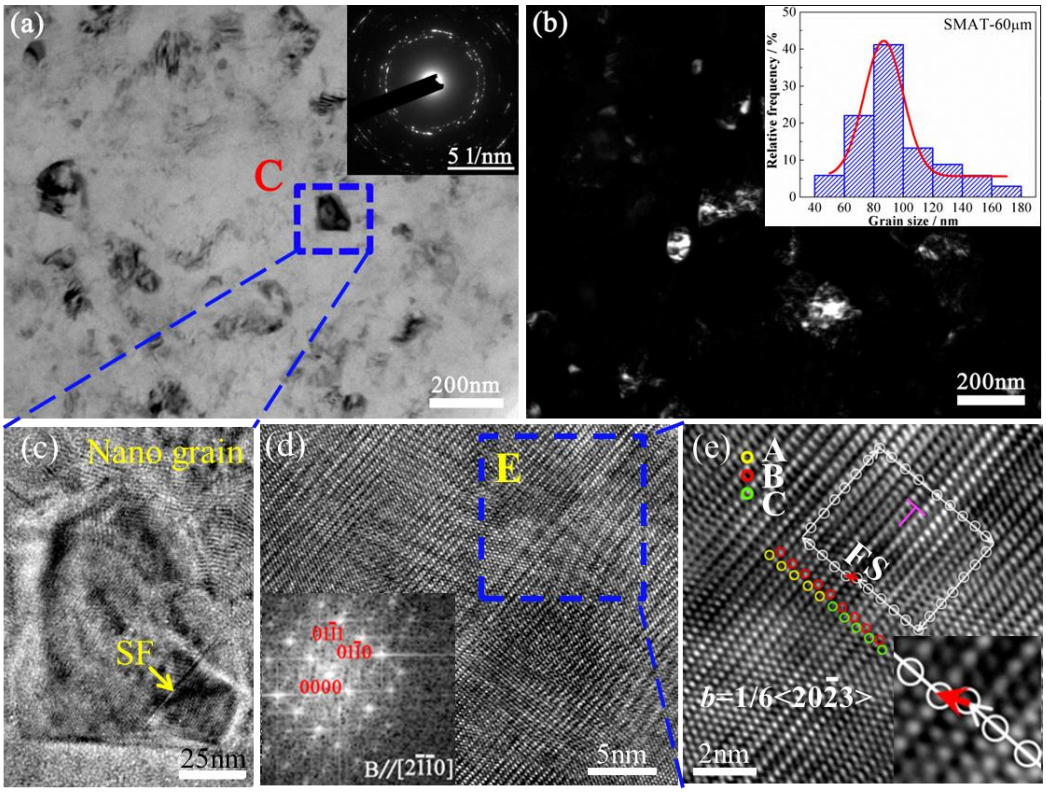

Fig.8 Microstructure of the SMAT-processed WE43 sheet observed at the depth of ~60 μm below the surface: (a) TEM bright field image and the corresponding SAED patterns inserted; (b) TEM dark field image and histogram of distribution of grain size inserted; (c) magnified image of the region C marked by box in (a); (d) HRTEM image of SF marked by arrow in (c) and the corresponding FFT image inserted; (e) IFFT image of SF in the region E marked by box in (d).

At last, Fig. 9(a-b) and Fig. 9(c-d) give the TEM images in the depth layer ~ 30 μm and the topmost surface layer, respectively, of the SMAT-processed WE43 alloy. The average grain size is further uniformly decreased to ~53 nm in the depth layer of ~30 μm and eventually ~40 nm in the topmost surface layer, as the statistics made in Fig. 9(b) and Fig. 9(d). Meanwhile, the diffraction spots are almost well-defined continuous rings in Fig. 9(a) and Fig. 9(c), stating the refined nanograins in these two layers having high-angles boundaries with random orientations [49]. Therefore, the inhomogeneous intense strains during the SMAT process finally successfully fabricate the gradient nanostructured WE43 alloy with the supersaturated solid-solution nanograined surface layer.

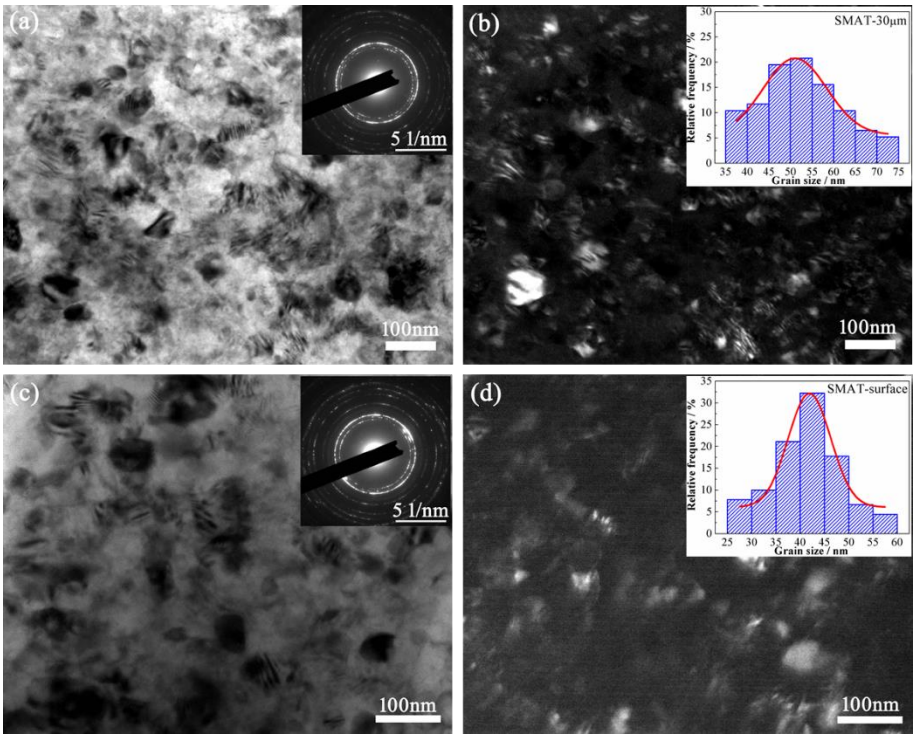

Fig. 9 Microstructure of the SMAT-processed WE43 sheet observed at the depth of ~30 μm (a, b) and the topmost surface (c, d): (a) and (c) TEM bright-field images and SAED patterns inserted; (b) and (d) TEM-dark field images and histograms of distribution of grain size inserted.

3.3 Enhanced mechanical properties of SMAT-processed WE43 alloy

Fig. 10(a) shows the microhardness evolution along the depth direction from the topmost surface to the matrix of the both-side SMAT-processed WE43 specimen, together with the corresponding average grain size statistically determined in the light of our experimental characterization. The measured microhardness value is ~82.5 HV in the near matrix depth layer, which is gradually monotonically increased to ~117.5 HV at the topmost surface layer, by a factor of ~42%. Based on microstructural evolution results of the gradient nanostructured layer with a thickness of ~120 μm, the corresponding hardening mechanisms should be composed of Hall-Petch grain boundary hardening, dislocation hardening, and solid solution hardening. Accordingly, Fig. 10(b) lists the estimated contributions of each hardening factor at various depth layers, which will be quantitatively discussed in detail in Section 4.2. It can be clearly seen that the contribution of grain size reduction-induced grain boundary hardening increases more obviously than that of dislocation density hardening, with the depth decreases. While the estimated value of solid solution hardening remains unchanged as the second phase is completely dissolved into the α-Mg matrix phase from the depth of ~120 μm onwards. Therefore, it can be concluded that under the present experimental conditions, the factor of grain

refinement plays a prominent role in the hardening effects of the SMAT-processed WE43 alloy.

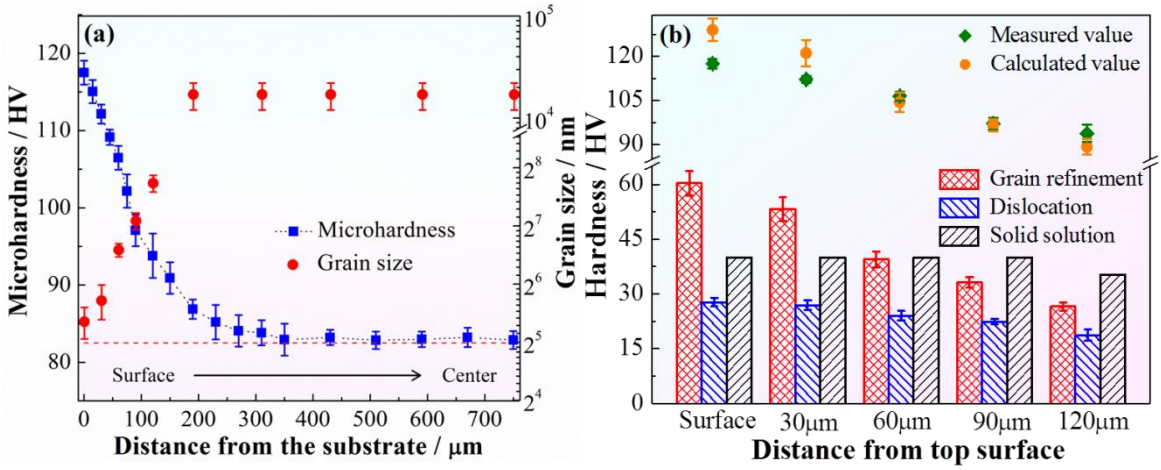

Fig.10 (a) Variation of Vickers microhardness across the thickness direction of SMAT-processed WE43 sheet with different depths from the topmost surface (the red dashed line indicates the microhardness of initial as-extruded alloy); (b) Contribution of grain refinement and dislocation density to hardness for SMAT-processed WE43 sheet within different depth layer, and the scattered dots of green rhombus and orange circle respectively denote the measured values and calculated values of overall microhardness at selected layer.

In addition, Fig. 11(a) presents the engineering stress-strain curves of as-extruded and SMAT-processed WE43 alloys tested along with ED at ambient temperature. Their corresponding tensile yield strength (TYS), ultimate tensile strength (UTS) as well as the elongations to failure are summarized in Fig. 11(b). The as-extruded WE43 alloy exhibits a TYS of ~180 MPa and UTS of ~250 MPa, which are remarkably improved in SMAT-processed specimen by around 1.6 times and 1.8 times to ~280 MPa and ~435 MPa, respectively. Meanwhile, the elongation to failure of SMAT-processed specimen is slightly decreased from ~14.5% to ~11.0%. Besides, the uniform elongation ε_u that relates to the maximum stress in Fig. 11(b) can be determined by the Considère criterion [50]:

$$\sigma_T = \left(\frac{\partial \sigma_T}{\partial \varepsilon_T}\right)_{\dot{\varepsilon}} \quad (3),$$

where σ_T represents the true stress, ε_T is the true strain, and the term of $\left(\frac{\partial \sigma_T}{\partial \varepsilon_T}\right)_{\dot{\varepsilon}}$ is the work hardening rate θ. Noticeably, the intersection point between the work hardening rate curve and the true stress curve should be the point of plastic instability [50], Accordingly, the uniform elongation ε_u of SMAT-processed WE43 alloy is ~10.4% as shown in Fig. 14(b) in the next section, which is slightly reduced as compared to the as-extruded one.

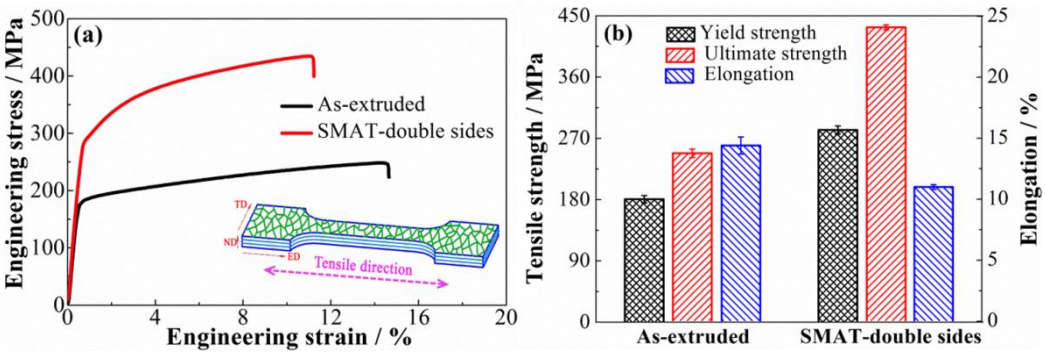

Fig. 11 The mechanical properties for as-extruded and SMAT-processed WE43 alloys tested at ambient temperature: (a) engineering stress-strain curves and (b) comparison of tensile strength and elongation.

The detailed SEM characterization of fracture surface morphologies of as-extruded and SMAT-processed WE43 alloys are shown in Fig.12. Fig. 12(a-b) shows that the fracture surface of the as-extruded WE43 sheet is quite rough with plenty of elongated irregular dimples, indicating that a typical ductile fracture governed by the nucleation and linkup of microvoids accounts for the shear deformation behavior. The cross-sectional tensile fracture morphology of the SMAT-processed WE43 sheet is depicted in Fig. 12(c), in which two typical regions with distinct morphology features are marked by a transition dashed line. It is noted that such a transition is extended to the depth layer of ~120 μm below the topmost surface, which is in good agreement with the observed microstructure evolution during SMAT. Fig. 12(d-e) shows the fracture surface corresponding to the central matrix coarse-grained zone of the SMAT-processed specimen, displaying a similar morphology to the as-extruded one accompanied by numerous large dimples with sizes of 5-10 μm. However, the dimples in the fracture surface of the refined layer, as seen in Fig. 12(f-g), become denser, smaller, and shallower as compared to the central matrix coarse-grained zone in the SMAT-processed specimen. This is attributed to the discrepancy of plastic deformation mechanisms between nanograins and coarse grains. Compared to the coarse-grained matrix controlled by the interactions of intra-grain dislocations activities, the significantly enhanced volume fraction of grain boundary in the refined layer would severely suppress these dislocation activities. Alternatively, it would cause numbers of voids to nucleate and grow up at grain boundaries with high-stress concentration, and then generate the smaller dimples in the refined layer with smaller grain size [51].

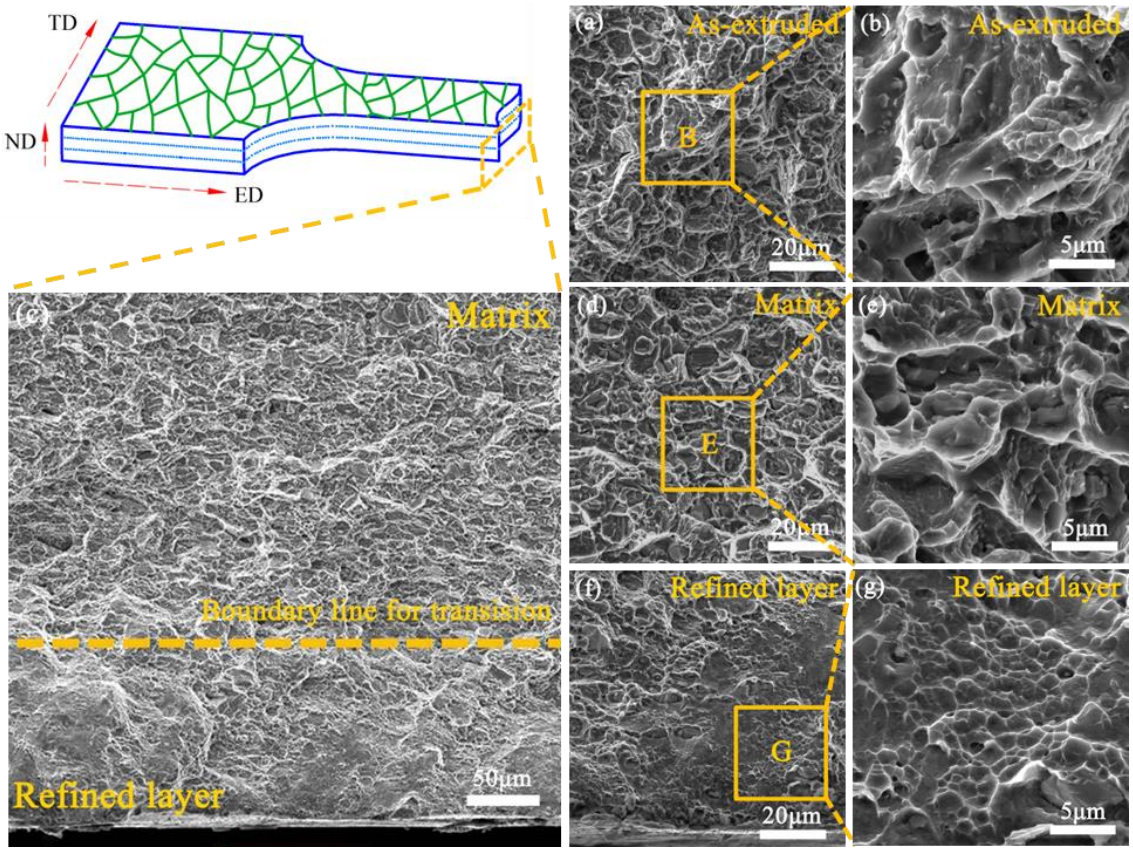

Fig. 12 SEM micrographs of the fracture surface morphologies after tensile tests: (a) and (b) as-extruded WE43 sheet; (c) SMAT-processed WE43 sheet: (d) and (e) the central zone; (f) and (g) the refined layer zone.

4. Discussion

Our detailed experimental characterizations have dissected the grain refinement process along the depth direction of the SMAT-processed WE43 alloy and corresponding significant enhanced mechanical properties. More specifically, (i) The microstructures of the SMAT-produced gradient nanostructured WE43 alloy are gradually changed from coarse grains with dislocation cells and pile-ups, ultrafine subgrains, and finally the randomly oriented nanograins with the grain size of ~40 nm from the matrix to the topmost surface, in which the dissolution of the Mg_3RE second phase into α-Mg matrix phase within the gradient nanostructured layer is particularly well-verified. (ii) The SMAT-processed WE43 alloy possesses an extraordinary strain hardening with an outstanding combination of strength and ductility among all reported WE43 alloys. The SMAT-induced effective grain refinement in WE43 alloy with the dissolution of the second phase and corresponding plastic strengthening mechanisms responsible for the significantly enhanced mechanical properties will be elaborated in this section.

4.1 The gradient refinement mechanisms during the SMAT process

Based on the microstructural evolution characterizations at different depth layers, the creation of gradient nanostructure in WE43 alloy relies primarily on DRX during SMAT process at room temperature, and massive dislocation activities are observed. Fig. 13(a) schematically summarizes the several representative stages of the DRX-induced grain refinement process of SMAT-processed WE43 alloy. Initially, the as-extruded WE43 alloy prior to the SMAT process has an equiaxed coarse-grained structure. Once the SMAT process is started, dislocation slip systems in WE43 alloy would be first triggered to form dislocation pile-ups or/and dislocation walls within these original coarse grains. At the subsequent stage, continuous increasing strain and strain rate are accompanied with the increased population of dislocations, and then the ultrafined subgrains with low angle grain boundaries (LAGBs) are gradually formed by dislocation interactions, as revealed by XRD analysis in Fig. 4. Noticeably, the re-dissolution of the second phase into the α-Mg matrix occurs in this stage, leading to a supersaturated solid solution phase, which might induce extra local strain/stress concentration fields for the dislocation accumulation [49]. Finally, equiaxed nanograins with random orientations are commonly produced in the top surface layer with the most severe plastic strain and strain rate. Accordingly, as shown in Fig. 13(b), such kind of sandwich-like gradient nanostructure transiting from micrometer to submicron-nanometer scales has been realized in the SMAT-processed WE43 alloy.

The similar intensive strain/strain rate-induced refinement with the dissolution of the second phase into matrix phase has also been reported in various alloys during the SSPD processes, such as AA7055 aluminum alloy by surface abrasion, AA2024 and AA7150 aluminum alloys by ultrasonic shot peening (USSP), and steels by SMAT, etc. [52-54]. In essence, the dissolution of the second phase during the SMAT process can be thought of as the progress of mass transfer with the redistribution of alloying elements. It can be probably understood by the interactions between the precipitates and defects at the interface or interior of the precipitates. On one hand, the profuse moving dislocations during the SMAT process would substantially cut through and significantly refine the precipitates, thus increasing the precipitate-matrix interfaces. Due to the Gibbs-Thomson effect, accordingly, these refined and deformed precipitates with higher surface energy are thermodynamically unstable for the dissolution into the matrix. On the other hand, the refined nanostructure can provide more effective channels, such as dislocations, vacancies, and non-equilibrium grain boundaries, to accelerate the

atomic diffusion for the dissolution of RE atoms into the α-Mg matrix to form a supersaturated solid solution [55].

It is worth noting that the average grain size in the topmost surface layer of the SMAT-processed WE43 alloy in this study is smaller than that of various counterparts (range of 80 nm-3 μm) subjected to other types of SPD techniques [56-63]. An empirical formula of $(d_{rec}/d_{init}) = 10^3 \times Z^{-1/3} = 10^3 \times \{\dot{\varepsilon} \times \exp(Q/RT)\}^{-1/3}$ has been employed to describe the relationship between the refined grain size d_{rec} by recrystallization and Zener-Holloman (Z) parameter, where the d_{init} means the initial grain size, R is gas constant, T is the absolute temperature, $\dot{\varepsilon}$ represents the plastic strain rate and Q is taken to be the activation energy for the lattice diffusion of magnesium (136 kJ/mol) [64]. It has been well-known that SMAT processing can achieve an extremely high plastic strain rate of 10^4-10^5 s^{-1} [65, 66], leading to a high efficiency in the microstructure refinement. As compared to the other SMAT-processed conventional non-RE magnesium alloys, the present investigated WE43 alloy under similar deformation conditions exhibits a stronger substantial grain refinement to the nanoscale, indicating that the introduction of the high RE content and preexisting dispersed precipitate particles exert pronounced effects in pinning dislocations and subsequently facilitating the extra refinement. It is well known that HCP crystal structures have limited slip systems, and the critical resolved shear stress (CRSS) for the non-basal slips is obviously larger than that for the basal slip. Therefore, basal slip would be first activated to accommodate the plastic deformation, usually resulting in a typical basal texture [30]. Noticeably, the addition of RE elements into Mg alloy could effectively reduce the CRSS of the non-basal slips, e.g., prismatic slip and/or pyramidal slip, thus decreasing the plastic anisotropy and improving the plasticity of HCP crystals to form a relative randomly structure [30]. Accordingly, the ultrafine subgrains with LAGBs can be further refined to the randomly oriented nanograins with HAGBs in the topmost surface of the SMAT-processed WE43 alloy with the dissolution of RE atoms-induced supersaturated solid solution.

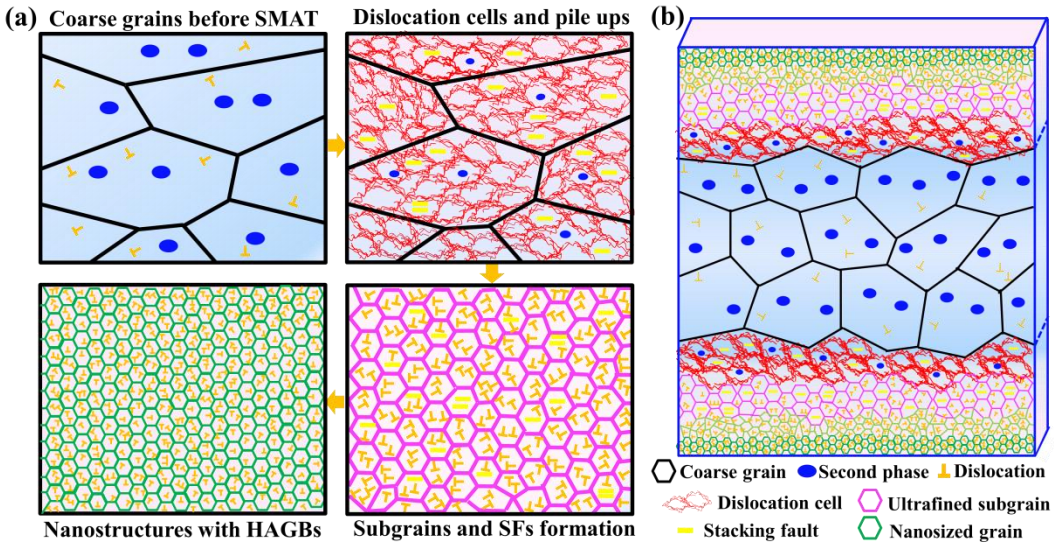

Fig.13 (a) Schematic illustration of the DRX refining process of WE43 alloy during SMAT; (b) the gradient structure produced by SMAT.

4.2 Strengthening mechanisms of the SMAT-processed specimen

Based on our XRD and TEM results in Section 3.2, the original second phase particles are almost completely broken up and dissolved into the α-Mg matrix from the depth layer of ~120 μm to the topmost surface layer of the SMAT-processed WE43 alloy. It means that the precipitation hardening effect could be almost neglected and replaced by the solid solution hardening within the above gradient depth layer. In addition, the texture effect can also be ignored as it becomes a random orientation during the SMAT process. In general, the relationship between microhardness *HV* and yield strength σ_y can be expressed by the following equation [67]:

$$HV = C\sigma_y \quad (4),$$

where *C* is a constant about ~0.3, and the units of Vickers hardness are taken as HV.

As shown in Fig. 10(b), therefore, the variation of the Vickers microhardness at various layers along the depth direction can be estimated by summing up the following several hardening factors: the grain boundary hardening ($\triangle HV_{GB}$), dislocation hardening ($\triangle HV_D$) and solid solution hardening ($\triangle HV_{SS}$):

$$HV = HV_0 + \triangle HV_{GB} + \triangle HV_D + \triangle HV_{SS} \quad (5),$$

where HV_0 refers to the microhardness of un-deformed pure Mg, which equals about 6.0 HV [67]. The Hall-Petch relationship is applied for the estimation of grain boundary hardening, in which the hardness contribution is proportional to the inverse square of the grain size [67]:

$$\triangle \mathrm{HV}_{GB} = Ck_{HP}d^{-1/2} \quad (6),$$

where k_{HP} is the Hall-Petch coefficient taken as ~40.7 MPa / μm$^{-1/2}$ for Mg, and d is the mean grain size at each depth layer. The dislocation hardening contribution can be predicted from existing models [67] as follows:

$$\triangle HV_D = CM\alpha_1 Gb\sqrt{\rho} \quad (7),$$

where M is the Taylor factor, α_1 is a constant of 0.3, b is Burgers vector (0.3197 nm for Mg), G is the shear modulus (17.7 GPa for Mg), and ρ is the original dislocation density of different depth layers in SMAT-processed WE43 alloy. The solid solution hardening contribution from two or more solute alloying elements can be described as the following equation [68]:

$$\triangle HV_{SS} = C(\sum k_i^{3/2} c_i)^{2/3} \quad (8),$$

where c_i is the concentration of the corresponding solute atom within the matrix, and k_i is the factor related to the individual solute element. As the Y, Nd and Gd elements have similar physicochemical properties involving atomic size and shear modulus, the values of k_Y, k_{Nd} and k_{Gd} are set equally in the SMAT-processed WE43 alloy, thus the calculation of solid solution hardening can be rewritten as the following formula:

$$\triangle HV_{SS} = Ck_{RE}c_{RE}^{2/3} \quad (9),$$

where the k_{RE} is set as 1856 MPa(at.%)$^{-2/3}$ [68], and c_{RE} is the total atomic concentration of RE elements in the α-Mg matrix phase. According to the EDS analysis in Fig.1(d), Fig. 6(k) and Fig. 7(f), the total atomic concentrations of RE elements are 1.40 at.%, 1.59 at.% and 1.92 at.% in as-extruded, at the depth layer of ~120 μm and ~90 μm in the SMAT-processed samples, respectively. Accordingly, it denotes the solid-solution hardness of ~ 32.3 HV, ~ 35.2 HV, and ~ 40.0 HV, respectively. Apparently, the re-dissolution of second phase and corresponding supersaturated solid solution during SMAT process can increase the solid solution hardening effect. It should be noted that re-dissolution of Mg_3RE second phase is totally completed from the depth of ~ 90 μm to the topmost surface in the SMAT-processed samples. Therefore, the RE concentrations in these supersaturated solid solutions remain constant, resulting in the unchanged hardness contribution from the depth layer of ~90 μm to the topmost surface layer. Based on the variations of grain size and dislocation density along the depth direction of the SMAT-processed specimen, as shown in Fig. 10(a) and Fig. 4(b), the corresponding grain boundary and dislocation hardening factors can be obtained, respectively. Fig. 10(b) shows the perfect agreement between the estimated and measured values of microhardness in several

representative depth layers in SMAT-processed WE43 alloy. It is obvious to distinguish that the significant grain refinement together with extra high dislocation density determines a remarkable increase of microhardness within the SMAT-deformed area.

The strain-hardening curves of θ against (σ_T-σ_{TYS}) for these two specimens are plotted and compared in Fig. 14(a). It can be seen that both of the original and SMAT-processed WE43 alloy sheets possess a similar trend in tensile behavior following by a plastic strain hardening model with negative slopes of strain hardening rate ($d\theta/\sigma_T$-$\sigma_{TYS} < 0$ as marked by arrows), meaning that deformation mechanism of multiple dislocations slipping dominates the strain hardening in tension [69]. Noticeably, the slope of strain hardening rate of the SMAT-processed specimen is higher as compare to the as-extruded one, implying that a better work hardening effect is generated from gradient strain in proportion to the density of geometrically necessary dislocations (GNDs), thus superior stress and reasonable ductility can be simultaneously obtained.

In addition, the work/strain hardening exponent *n* of the uniform plastic deformation stage in uniaxial tensile curve can be empirically expressed by a power-law hardening equation shown as follow [70, 71]:

$$\sigma_T = K\varepsilon_T^n \quad (10),$$

where *K* is the material constant indicating the increment in strength due to work hardening with ε_T=1. Such parameter *n* in gradient structured WE43 alloy is roughly obtained by linearly fitting the slop of $\ln\sigma_T$-$\ln\varepsilon_T$ plot (~0.21), and it is higher than that of as-extruded counterpart with coarse grains (~0.15) by a factor of ~40%. Moreover, the tensile test was only performed on the gradient layer with a thickness of ~200 μm. Obviously, the gradient layer sample exhibits a highest strength of ~560 MPa but a lowest elongation of ~2.8% as the inset shown in Fig. 14(b) Therefore, the double-side SMAT-processed specimen possesses the superior combination of strength and ductility by the cooperative effects of strain/stress partitioning and strain gradient between different domains.

The work hardening capacity H_C is also defined as a ratio of ($\sigma_{TUTS} - \sigma_{TYS}$) to σ_{YS} [70, 71] in Eq. (11):

$$H_C = \frac{\sigma_{TUTS} - \sigma_{TYS}}{\sigma_{TYS}} \quad (11),$$

where σ_{TUTS} and σ_{TYS} are ultimate tensile strength and yield strength achieved from the true stress-strain curve, respectively. For the as-extruded WE43 alloy, the H_C value is ~0.39, whereas it is

enhanced to ~0.55 after SMAT processing due to the formation of gradient structure. Therefore, the parameters for evaluating the work hardening behavior of wrought WE43 alloys can be summarized in Table 2.

Table 2 The mechanical properties of WE43 alloy in present study

Samples	σ_{TYS}/ MPa	σ_{TUTS}/ MPa	ε_u/ %	n	H_C
As-extruded	180	250	13.2	0.15	0.39
SMAT-processed	280	435	10.4	0.21	0.55
Gradient layer	368	560	2.8	0.20	0.52

Notably, the cooperative effects of the grain boundary, dislocation, and solid-solution hardening factors in heterogeneous gradient nanostructured SMAT-processed WE43 alloy are also responsible for the better strain hardening superior to the as-extruded specimen. The gradient nanostructured WE43 sheet can be viewed as several layers with gradient grain sizes and dislocation densities from the less deformed center layer to the severely deformed top layer. Based on the results shown in Fig. 14(a), the strain hardening behavior of both as-extruded and SMAT-processed alloys can be ascribed to the well-known stage III commonly found in the polycrystalline Mg alloys, where the work hardening rate θ can be described by a Voce equation as follow [72, 73]:

$$\theta = \theta_0^{\mathrm{III}}\left(1 - \frac{\sigma_T}{\sigma_s}\right) \quad (12),$$

where θ_0^{III} is a hardening limit extrapolate to σ_T=0, and σ_s is a saturation stress extrapolated to θ=0. Besides, the parameters of θ_0^{III} and σ_s are expressed by the equations (13) and (14), respectively [73].

$$\theta_0^{\mathrm{III}} = \frac{1}{2}M^2\alpha_1 G k_1 \quad (13)$$

$$\sigma_s = \frac{M\alpha_1 G k_1}{k_2} \quad (14),$$

where k_1 and k_2 are material constants [73].

In fact, the work hardening behavior during the tensile test can be controlled by the dislocation evolution of the competition of storage and annihilation/rearrangement. The classical model proposed by Mecking et al. [72-74] are assumed to superimpose in an additive manner to describe the variation of total dislocation density ρ_t with tensile plastic deformation strain ε_p through the following equation:

$$\frac{\partial \rho_t}{\partial \varepsilon_p} = k_1\rho_t^{1/2} - k_2\rho_t + k_D \quad (15),$$

where the first term $k_1\rho_t^{1/2}$ is associated with statistical storage of moving dislocations during tensile

deformation, the second term $k_2\rho_t$ is related to dynamic recovery depending on strain rate and solute concentration, and the third one k_D represents the athermal storage of dislocations at boundaries determined by the grain size. The recent research pointed out that the third term is related to the extra accumulation of GNDs [74]. Based on the work hardening curves in Fig. 14(a) and the Eqs.(12-14), the value of k_1 is increased from ~0.05 in original specimen to k_1 ~0.15 in SMAT-processed specimen, while the value of k_2 is also varied from ~1.87 to ~6.46 induced by the introduction of gradient structure deriving from the dislocation strain field interaction [71]. During the uniaxial tensioning experiment, due to the complex stress state near the domain interfaces among different depth layers, the resultant incompatibility heterogamous gradient strain has to be accommodated by GND pile-ups, which causes long-range hetero-deformed induced stress and then produces a strong strain hardening with good ductility [75]. Besides, after SMAT processing, the supersaturated solid solution with the increased solute atoms RE into Mg alloys are supposed to further promote the <c+a> dislocations whereas suppressing twin nucleation [30, 74]. The activation of <c+a> dislocations slipping through accelerating cross-slipping is often believed to not only accommodating c-axis plastic deformation and alleviate stress concentration at grain boundaries, but also increases the flow stress in Mg during the deformation [74], which may be another factor responsible for the strong work hardening in the SMAT-processed WE43 alloy. It is also supported by the fracture characteristics in Fig. 12, which illustrates that a prominent inhomogeneous deformation in the overall sheet is governed by two distinct operating fracture mechanisms. Coarse grains and nanograins in heterogeneous structure would be mutually constrained and influenced beneficially for suppressing strain localization and eventually causing a combination of high strength and good ductility. Furthermore, the tensile elongation and the σ_{UTS}-σ_{YS} values of different Mg wrought Mg alloys are also displayed in Fig. 14(c) [74]. With comparison, the present gradient layer is located at the upper corner, especial for the WE43 alloy processed by SMAT with double sides has a superior mechanical property with better hardening ability and reasonable plasticity.

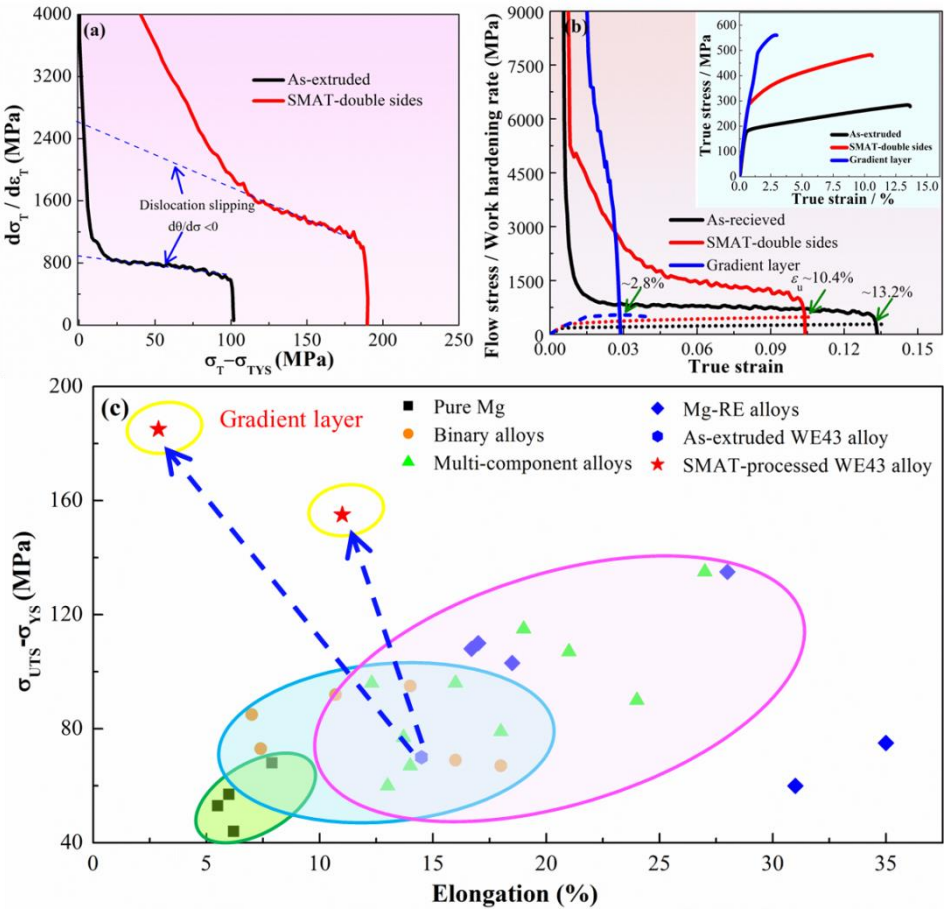

Fig.14 (a) work hardening rate curves using θ-(σ_T-σ_{TYS}) plot obtained from true stress-strain curves; (b) instantaneous work hardening rate and the true stress curves against the true strain, and (c) Comparison of elongation and (σ_{UTS}-σ_{YS}) values of different wrought alloys [74].

At last, Fig. 15(a) and (b) compare the mechanical properties of the SMAT-processed WE43 alloy in this study with other various available SMAT-processed Mg alloys and WE43 alloys by some other SPD techniques, respectively. The strengths of these SMAT-processed Mg alloys, e.g., AZ31 and Mg-3Gd alloys, are relative lower than 350 MPa with tensile elongation of ~4%-17%. Obviously, the SMAT-processed WE43 alloy in the present case has a superior strength and good ductility, as shown Fig. 15(a). Fig. 15(b) shows that the casting and heat-treated WE43 alloys located near the lower end of the spectrum exhibit inferior mechanical properties [57, 59, 62, 76-79], whereas the conventional thermomechanical processing (e.g., extrusion and rolling followed by ageing) can make a limited enhancement [6, 56, 58, 61-63, 80-86]. It is remarkable that due to the imposed intensive plastic strains, the SPD-processed WE43 alloys fall in the upper side of the thermomechanical processed counterparts [56, 57, 59, 62, 63, 76-79, 84, 85, 87, 88]. Interestingly, the introduction of pre-deformation prior to the typical SPD processing is beneficial to promote the tensile elongation despite the influence on the strength increment is not significant [58, 60-62]. Clearly, the so-called similar banana-like shaped

region can be marked out in the WE43 alloys with homogenous microstructure, indicating that the strength and ductility are mutually exclusive. However, when the as-extruded WE43 alloy suffered the SMAT, there is a noticeable increase in strength with almost negligible sacrifice in elongation. As expected, the mechanical properties of WE43 alloy are closely related to the distributions of grain size profile, which can be controlled by the imposed plastic strains and deformation temperature. Moreover, a power-law equation is usually applied to express the degree of the grain-size gradient in gradient structural metals [66]. The average grain size d and normalized position x along the thickness of the plate follow the empirical relation of $\mathrm{d} = d_{max} - (d_{max} - d_{min})(1-x)^m$, where d_{max} and d_{min} denote the minimum and maximum values of grain sizes, respectively, and m represents the power index for the grain size distribution to describe the gradient degree. It has been proved that the gradient samples with the index m equal to 3-5 exhibits a higher yield strength and better elongation as compared to the coarse-grained counterparts [66]. In the current case for the SMAT-processed WE43 alloy, the value of power index m is approached to ~5, meaning that this structure can achieve an acceptable strength-ductility synergy.

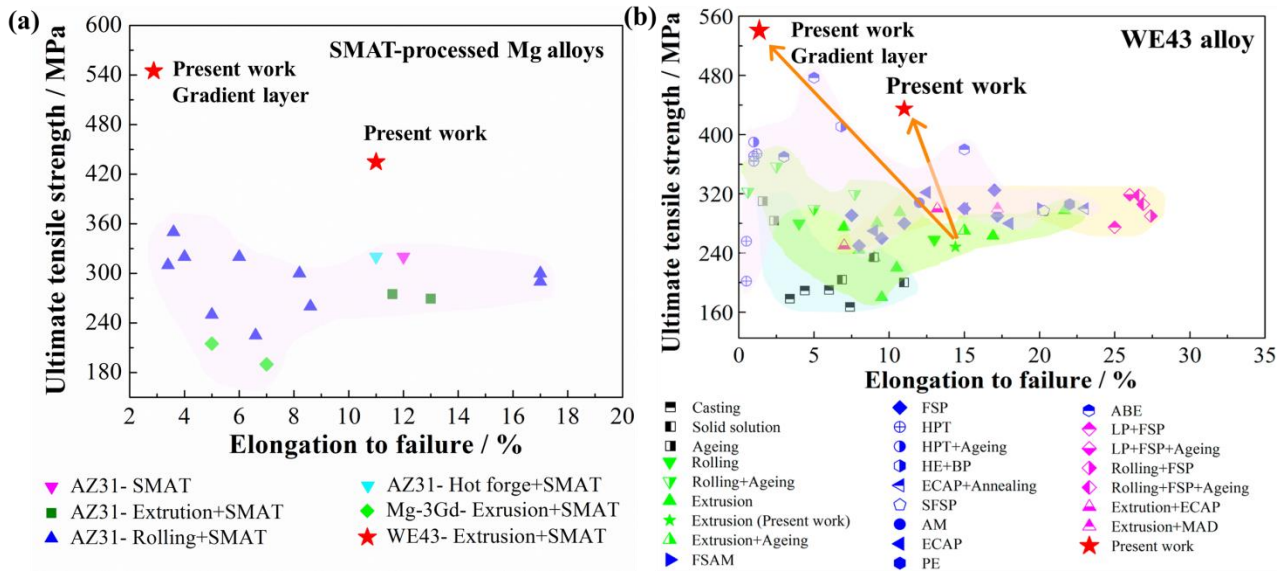

Fig. 15 (a) Comparisons of the ultimate tensile strength and elongation in various available Mg alloys processed by SMAT[17, 19-23, 31]; (b) Comparisons of the ultimate tensile strength and elongation in WE43 Mg alloy under different processing conditions involving casting [57, 59, 76, 77], heat treatment [59, 78, 79], traditional thermomechanical processing [6, 56, 58, 61-63, 80-86] and SPD methods. (FSP represents friction stir processing [56, 57, 60, 61, 76]; FSAM represents friction stir additive manufacturing [85]; SFSP represents submerged friction stir processing; LP represents laser processing [60, 76]; ECAP represents equal channel angular pressing [58, 59, 88]; ABE represents accumulative back extrusion [84]; MAD represents multiaxial deformation [62]; HPT represent high pressure torsion [63, 79]; HE+BP represents hydrostatic extrusion with back pressure [87]; AM represents additive

manufacture [77]; PE represents power extrusion [77].

Conclusions

In the present work, the gradient nanostructured WE43 alloy is successfully prepared by the SMAT technique at room temperature. The microstructure evolution for the refinement process and corresponding strengthening mechanisms have been discussed in detail. The main conclusions can be drawn as follows:

(1) With increasing the plastic strain and strain rate along the depth direction during the SMAT process, the fabricated gradient nanostructured WE43 alloy can be simply divided into three typical stages from the inner matrix to the topmost surface layer, i.e., numerous dislocation pile-ups or/and dislocation walls firstly generated within the original coarse grains, and the ultrafine subgrains with LAGBs, and finally the nanocrystallized structure with HAGBs through dislocation accumulation and arrangement. The refinement process is also accompanied with a texture weakening effect, leading to nearly randomly orientated nanograins with the average grain size of ~40 nm in the topmost surface layer. Particularly, the second phase is inevitably sheared and completely dissolved into the α-Mg matrix, leading to a supersaturated solid solution nanostructure in the refine gradient layer.

(2) The gradient refinement in the SMAT-processed WE43 alloy results in the gradual increase of the microhardness along the depth direction, achieving a maximum microhardness value of ~117.5 HV at the topmost surface layer. Owing to the outstanding heterogeneous gradient nanostructured strain hardening effect, as compared to the original as-extruded WE43 alloy, the SMAT-processed WE43 alloy demonstrates the enhanced comprehensive mechanical properties with an ultimate tensile strength of ~435 MPa and reasonable ductility of 11.0 %. The tensile fracture feature of the gradient nanostructured WE43 alloy also shows the multi-scaled dimples according to the variation of grain size along the depth direction, signifying the high strength-ductility synergy.

(3) Several hardening factors, including grain size reduction-correlated grain boundary hardening, dislocation hardening, and solid-solution hardening, are quantitatively estimated along the depth direction in the gradient refined layer, which is well agreed with the measured results. Accordingly, these cooperative hardening effects in the present SMAT-processed WE43 contribute to an extraordinary mechanical property among the reported SMAT-processed Mg alloys and other SPD-processed WE43 alloys. This work is conducive to comprehensively understand the microstructure evolution and mechanical strengthening behavior of gradient nanostructured Mg-RE alloys.

Acknowledgements

This work was supported by National Natural Science Foundation of China (No. 51971187) and China Postdoctoral Science Foundation (No. 2019M653599). The authors also would like to express their sincere thanks to the financial support from Partner State Key Laboratories in Hong Kong from the Innovation and Technology Commission (ITC) of the Government of the Hong Kong Special Administration Region (HKASR), China and the PolyU Research Office (Project Code: 1-BBXA).

References:

[1] A.A. Luo, J. Magnes. Alloy 1 (2013) 2-22.
[2] Y.P. Pang, Q. Li, Int. J. Hydrogen Energ. 41 (2016) 18072-18087.
[3] Y.L. Guo, B. Liu, W. Xie, Q. Luo, Q. Li, Scripta Mater. 193 (2021) 127-131.
[4] Y.L. Guo, Q. Luo, B. Liu, Q. Li, Scripta Mater. 178 (2020) 422-427.
[5] Q. Luo, Y.L. Guo, B. Liu, Y.J. Feng, J.Y. Zhang, Q. Li, K. Chou, J. Mater. Sci. Technol. 44 (2020) 171-190.
[6] Z. Yang, J.P. Li, J.X. Zhang, G.W. Lorimer, J. Robson, Acta Metall. Sin. (Engl. Lett.) 21 (2009) 313-328.
[7] J.F. Song, J. She, D.L. Chen, F.S. Pan, J. Magnes. Alloy 8 (2020) 1-41.
[8] Z. Tian, Q. Yang, K. Guan, Z.Y. Cao, J. Meng, Rare Met (2020) 1-9.
[9] H.S. Jiang, M.Y. Zheng, X.G. Qiao, K. Wu, Q.Y. Peng, S.H. Yang, Y.H. Yuan, J.H. Luo, Mater. Sci. Eng. A 684 (2017) 158-164.
[10] S.H. You, Y.D. Huang, K.U. Kainer, N. Hort, J. Magnes. Alloy 5 (2017) 239-253.
[11] J.B. Liu, K. Zhang, J.T. Han, X.G. Li, Y.J. Li, M.L. Ma, J.W. Yuan, G.L. Shi, Rare Met. 39 (2020) 1273-1278.
[12] Q. Yang, S.H. Lv, Z.X. Yan, X.R. Hua, X. Qiu, J. Meng, Mater. Design 201 (2021) 109482.
[13] Y. Estrin, A. Vinogradov, Acta Mater. 61 (2013) 782-817.
[14] E. Ma, T. Zhu, Mater. Today 20 (2017) 323-331.
[15] X.L. Wu, Y.T. Zhu, Mater. Res. Lett. 5 (2017) 527-532.
[16] S.W. Xia, Y. Liu, D.M. Fu, B. Jin, J. Lu, J. Mater. Sci. Technol. 32 (2016) 1245-1252.
[17] G. Chen, J.W. Gao, Y. Cui, H. Gao, X. Guo, S.Z. Wu, J. Alloy Compd. 735 (2018) 536-546.
[18] H.L. Chen, J. Yang, H. Zhou, J. Moering, Z. Yin, Y.L. Gong, K.Y. Zhao, Metall. Mater. Trans. A 48 (2017) 3961-3970.
[19] X.C. Meng, M. Duan, L. Luo, D.C. Zhan, B. Jin, Y.H. Jin, X.X. Rao, Y. Liu, J. Lu, Mater. Sci. Eng. A 707 (2017) 636-646.
[20] X.W. Liu, Y. Liu, B. Jin, Y. Lu, J. Lu, J. Mater. Sci. Technol. 33 (2017) 224-230.
[21] J.L. Ning, B. Xu, M.S. Sun, C.Y. Zhao, Y.L. Feng, W.P. Tong, Mater. Sci. Eng. A 735 (2018) 275-287.
[22] J.H. Peng, Z. Zhang, P. Guo, Z. Liu, Y.Z. Li, W. Zhou, Y.C. Wu, Mater. Charact. 148 (2019) 26-34.
[23] L. Chen, F.P. Yuan, P. Jiang, J.J. Xie, X.L. Wu, Mater. Sci. Eng. A 694 (2017) 98-109.
[24] H.Q. Sun, Y.N. Shi, M.X. Zhang, K. Lu, Acta Mater. 55 (2007) 975-982.
[25] Y.H. Wei, B.S. Liu, L.F. Hou, B.S. Xu, G. Liu, J. Alloy Compd. 452 (2008) 336-342.
[26] M. Laleh, F. Kargar, J. Alloy Compd. 509 (2011) 9150-9156.
[27] L.H. Zhang, Y. Zou, H.T. Wang, L. Meng, J.B. Liu, Z.W. Zhang, Mater. Charact. 120 (2016) 124-128.
[28] N. Li, Y.D. Li, Y.X. Li, Y.H. Wu, Y.F. Zheng, Y. Han, Mater. Sci. Eng. C 35 (2014) 314-321.
[29] X.Y. Shi, Y.X. Li, X.Q. Zeng, Y. Liu, B. Chen, J. Lu, D.J. Li, J. Mater. Sci. Technol. 35(7) (2019) 1473-1478.
[30] K.K. Alaneme, E.A. Okotete, J. Magnes. Alloy 5 (2017) 460-475.
[31] X.Y. Shi, Y. Liu, D.J. Li, B. Chen, X.Q. Zeng, J. Lu, W.J. Ding, Mater. Sci. Eng. A 630 (2015) 146-154.

[32] Y. Liu, B. Jin, D.J. Li, X.Q. Zeng, J. Lu, Surf. Coat. Technol. 261 (2015) 219-226.
[33] S.W. Xia, J.M. Xu, Z.J. Wang, Y. Liu, J. Lu, J. Alloy Compd. 697 (2017) 282-286.
[34] Y. Zhang, L.L. Tan, Q.C. Wang, M. Gao, I.P. Etim, K. Yang, J. Mater. Sci. Technol. 51 (2020) 102-110.
[35] Y.H. Kang, Z.H. Huang, S.C. Wang, H. Yan, R.S. Chen, J.C. Huang, J. Magnes. Alloys 8 (2020) 103-110.
[36] A.V. Koltygin, V.E. Bazhenov, R.S. Khasenova, A.A. Komissarov, A.I. Bazlov, V.A. Bautin, Int. J. Min. Met. Mater. 26 (2019) 858-868.
[37] F. Bär, L. Berger, L. Jauer, G. Kurtuldu, R. Schäublin, J.H. Schleifenbaum, J.F. Löffler, Acta Biomater. 98 (2019) 36-49.
[38] M. Ferrari, L. Lutterotti, J. Appl. Phys. 76 (1994) 7246-7255.
[39] L. Lutterotti, S. Gialanella, Acta Mater. 46 (1998) 101-110.
[40] Y. Chen, N. Gao, G. Sha, S.P. Ringer, M.J. Starink, Acta Mater. 109 (2016) 202-212.
[41] T. Al-Samman, X. Li, Mater. Sci. Eng. A 528 (2011) 3809-3822.
[42] N. Stanford, Mater. Sci. Eng. A 527 (2010) 2669-2677.
[43] Q.M. Peng, J. Meng, Y.D. Li, Y.D. Huang, N. Hort, Mater. Sci. Eng. A 528 (2011) 2106-2109.
[44] H.L. Ding, X.B. Shi, Y.Q. Wang, G.P. Cheng, S. Kamado, Mater. Sci. Eng. A 645 (2015) 196-204.
[45] H.J. Lee, S.K. Lee, K.H. Jung, G.A. Lee, B. Ahn, M. Kawasaki, T.G. Langdon, Mater. Sci. Eng. A 630 (2015) 90-98.
[46] M.Q. Zhang, Y. Feng, J.H. Zhang, S.J. Liu, Q. Yang, Z. Liu, R.G. Li, J. Meng, R.Z. Wu, J. Mater. Sci. Technol. 35 (2019) 2365-2374.
[47] S.Q. Zhu, S.P. Ringer, Acta Mater. 144 (2018) 365-375.
[48] K. Wei, R. Hu, D.D. Yin, L.R. Xiao, S. Pang, Y. Cao, H. Zhou, Y.H. Zhao, Y.T. Zhu, Acta Mater. 206 (2021) 116604.
[49] W.T. Sun, X.G. Qiao, M.Y. Zheng, C. Xu, N. Gao, M.J. Starink, Mater. Design 135 (2017) 366-376.
[50] R.X. Zheng, T. Bhattacharjee, A. Shibata, T. Sasaki, K. Hono, M. Joshi, N. Tsuji, Scripta Mater. 131 (2017) 1-5.
[51] S. Majumdar, K.K. Ray, Metall. Mater. Trans. A 37 (2006) 3541-3553.
[52] S.S. Wang, J.T. Jiang, G.H. Fan, L. Yang, S.L. Dai, G.S. Frankel, L. Zhen, Mater. Charact. 98 (2014) 18-25.
[53] Q.Q. Sun, X.T. Liu, Q.Y. Han, J. Li, R. Xu, K.J. Zhao, Surf. Coat. Tech. 337 (2018) 552-560.
[54] S.D. Lu, Z.B. Wang, K. Lu, J. Mater. Sci. Technol. 26 (2010) 258-263.
[55] W.T. Sun, X.G. Qiao, M.Y. Zheng, Y. He, N. Hu, C. Xu, N. Gao, M.J. Starink, Mater. Sci. Eng. A 728 (2018) 115-123.
[56] A.M. Jamili, A. Zarei-Hanzaki, H.R. Abedi, P. Minárik, R. Soltani, Mater. Sci. Eng. A 690 (2017) 244-253.
[57] J. Li, D.T. Zhang, F. Chai, W. Zhang, Rare Met. 39 (2020) 1267-1272.
[58] N.S. Martynenko, E.A. Lukyanova, V.N. Serebryany, M.V. Gorshenkov, I.V. Shchetinin, G.I. Raab, S.V. Dobatkin, Y. Estrin, Mater. Sci. Eng. A 712 (2018) 625-629.
[59] L. Zhou, Y. Liu, J. Zhang, Z. Kang, Mater. Sci. Tech. 32 (2016) 969-975.
[60] N. Kumar, R.S. Mishra, N.B. Dahotre, R.E. Brennan, K.J. Doherty, K.C. Cho, Mater. Design 110 (2016) 663-675.
[61] N. Kumar, N. Dendge, R. Banerjee, R.S. Mishra, Mater. Sci. Eng. A 590 (2014) 116-131.
[62] S. Dobatkin, N. Martynenko, N. Anisimova, M. Kiselevskiy, D. Prosvirnin, V. Terentiev, N. Yurchenko, G. Salishchev, Y. Estrin, Materials 12 (2019) 3627.
[63] D.X. Liu, X. Pang, D.L. Li, C.G. Guo, J. Wongsa‐Ngam, T.G. Langdon, M.A. Meyers, Adv. Eng. Mater. 19 (2017) 1600698.
[64] C.I. Chang, X.H. Du, J.C. Huang, Scripta Mater. 57 (2007) 209-212.
[65] T.O. Olugbade, J. Lu, Nano Mater. Sci. 2 (2020) 3-31.
[66] X.Y. Li, L. Lu, J.G. Li, X. Zhang, H.J. Gao, Nat. Rev. Mater. 5 (2020) 706-723.
[67] M.J. Starink, X.Y. Cheng, S.F. Yang, Acta Mater. 61 (2013) 183-192.
[68] Y.H. Kang, X.X. Wang, N. Zhang, H. Yan, R.S. Chen, Mater. Sci. Eng. A 689 (2017) 435-445.
[69] C.J. Li, H.F. Sun, X.W. Li, J.L. Zhang, W.B. Fang, Z.Y. Tan, J. Alloy Compd. 652 (2015) 122-131.

[70] X.H. Chen, F.S. Pan, J.J. Mao, J.F. Wang, D.F. Zhang, A.T. Tang, J. Peng, Mater. Design 32 (2011) 1526-1530.
[71] N. Afrin, D.L. Chen, X. Cao, M. Jahazi, Scripta Mater. 57 (2007) 1004-1007.
[72] J.A. Del Valle, F. Carreño, O.A. Ruano, Acta Mater. 54 (2006) 4247-4259.
[73] Y. Estrin, H. Mecking, Acta Metall. 32 (1984) 57-70.
[74] G.M. Zhu, L.Y. Wang, J.F. Wang, J.F. Wang, J.S. Park, X.Q. Zeng, Acta Mater. 200 (2020) 236-245.
[75] X.L. Ma, C.X. Huang, W.Z. Xu, H. Zhou, X.L. Wu, Y.T. Zhu, Scripta Mater. 103 (2015) 57-60.
[76] G.H. Cao, D.T. Zhang, W. Zhang, C. Qiu, J. Alloy Compd. 636 (2015) 12-19.
[77] N.A. Zumdick, L. Jauer, L.C. Kersting, T.N. Kutz, J.H. Schleifenbaum, D. Zander, Mater. Charact. 147 (2019) 384-397.
[78] Y.H. Kang, D. Wu, R.S. Chen, E.H. Han, J. Magnes. Alloys 2 (2014) 109-115.
[79] E.A. Lukyanova, N.S. Martynenko, V.N. Serebryany, A.N. Belyakov, L.L. Rokhlin, S.V. Dobatkin, Y.Z. Estrin, Russ. Metall. 2017 (2017) 912-921.
[80] X.N. Gu, W.R. Zhou, Y.F. Zheng, Y. Cheng, S.C. Wei, S.P. Zhong, T.F. Xi, L.J. Chen, Acta Biomater. 6 (2010) 4605-4613.
[81] X.B. Zhang, G.Y. Yuan, L. Mao, J.L. Niu, W.J. Ding, Mater. Lett. 66 (2012) 209-211.
[82] X.H. Zhou, L. Jiang, P.P. Wu, Y. Sun, Y.D. Yu, G.Y. Wei, H.L. Ge, Int. J. Electrochem. Sci. 9 (2014) 304-314.
[83] L. Choudhary, R.K.S. Raman, J. Hofstetter, P.J. Uggowitzer, Mater. Sci. Eng. C 42 (2014) 629-636.
[84] S. Asqardoust, A.Z. Hanzaki, H.R. Abedi, T. Krajnak, P. Minárik, Mater. Sci. Eng. A 698 (2017) 218-229.
[85] S. Palanivel, P. Nelaturu, B. Glass, R.S. Mishra, Mater. Design 65 (2015) 934-952.
[86] M. Jahedi, B.A. McWilliams, P. Moy, M. Knezevic, Acta Mater. 131 (2017) 221-232.
[87] W. Pachla, A. Mazur, J. Skiba, M. Kulczyk, S. Przybysz, Arch. Metall. Mater. 57 (2012) 485-493.
[88] I.I. Papirov, M.A. Tikhonovsky, K.V. Kutniy, A.I. Pikalov, S.V. Sivtsov, L.A. Pizizhenko, V.S. Shokurov, Funct. Mater. 15 (2008) 139-143.